Journal of Non-Newtonian Fluid Mechanics 286 (2020) 104398

Contents lists available at ScienceDirect

Journal of Non-Newtonian Fluid Mechanics

journal homepage: www.elsevier.com/locate/jnnfm

A comparison of constitutive models for describing the flow of uncured styrene-butadiene rubber

Martin Řehoř [a], Alex Gansen [b], Clemens Sill [c], Patrycja Polińska [c], Stephan Westermann [c,1], Jean Dheur [c], Jörg Baller [b], Jack S. Hale [a,*]

[a] *Institute of Computational Engineering, University of Luxembourg, Faculty of Science, Technology and Medicine, Maison du Nombre, 6, Avenue de la Fonte, L-4364 Esch-sur-Alzette, Luxembourg*

[b] *Department of Physics and Materials Science, University of Luxembourg, Faculty of Science, Technology and Medicine, Campus Limpertsberg, 162a, Avenue de la Faïencerie, L-1511 Luxembourg, Luxembourg*

[c] *Goodyear Innovation Centre Luxembourg, Avenue Gordon Smith, L-7750 Colmar-Berg, Luxembourg*

ARTICLE INFO

MSC:
76A10

Keywords:
Viscoelasticity
Rate-type fluid models
Stress relaxation
Styrene-butadiene rubber
Experiment fitting

ABSTRACT

Uncured styrene-butadiene rubber (SBR) can be modelled as a viscoelastic material with at least two different relaxation mechanisms. In this paper we compare multi-mode constitutive models combining two viscoelastic modes (linear and/or nonlinear) in three possible ways. Our particular choice of the two modes was inspired by models originally developed to describe the response of asphalt binders. We select the model that best fits the experimental data obtained from a modified stress relaxation experiment in the torsional configuration of the plate–plate rheometer. The optimisation of the five model parameters for each model is achieved by minimising the weighted least-squares distance between experimental observations and the computer model output using a tree-structured Parzen estimator algorithm to find an initial guess, followed by further optimisation using the Nelder–Mead simplex algorithm. The results show that the model combining the linear mode and the nonlinear mode is the most suitable variant to describe the observed behaviour of SBR in the given regime. The predictive capabilities of the three models are further examined in changed experimental and numerical configurations. Full data and code to produce the figures in this article are included as supplementary material.

1. Introduction

Styrene-butadiene rubber (SBR) is the most widely used synthetic rubber and forms a key constituent of many industrial products. It is important to understand its mechanical behaviour in order to accurately predict its response in various settings, both in manufacturing during extrusion, see Rauwendaal [1], and *in situ* in a finished automotive tyre, see Nakajima [2].

The prediction of the viscoelastic behaviour of rubbers such as SBR is a research area spanning back decades with many contributions. A recent overview with a particular focus on filled SBR compounds was given by Carleo et al. [3]. Montes et al. [4] studied the behaviour of carbon black compounds in various shear flow histories, e.g. stress relaxation and transient shear flow. Ovalle Rodas et al. [5] examined SBR compounds under cyclic loading in a wide range of temperatures. In the context of extrusion, Jugo Viloria et al. [6] characterised the flow instabilities of pure SBR and SBR compounds filled with silica using capillary rheometry. Regarding constitutive modelling, the topic of this paper, Choi and Lyu [7] and later on Talib and Ertunç [8] studied the performance of the Phan–Thien–Tanner model and the Giesekus model, respectively, in a capillary geometry for predicting swell at the die exit. An increasingly popular theoretical framework for developing constitutive models uses fractional derivatives, see e.g. Shabani et al. [9]. Models based on fractional derivatives can reproduce experimental data exhibiting multiple time scales with fewer parameters than their counterparts using the standard derivative. However, their practical use in three-dimensional numerical simulations is complicated by the inherently non-local nature in time, see e.g. Alotta et al. [10].

In this contribution we demonstrate the performance of three constitutive models for SBR built on recent developments in thermodynamically consistent viscoelastic rate-type fluid models from Málek

---

[*] Corresponding author.

E-mail addresses: martin.rehor@uni.lu (M. Řehoř), alex.gansen@uni.lu (A. Gansen), clemens_sill@goodyear.com (C. Sill), patrycja_polinska@goodyear.com (P. Polińska), stephan_westermann@goodyear.com (S. Westermann), jean.dheur@goodyear.com (J. Dheur), joerg.baller@uni.lu (J. Baller), jack.hale@uni.lu (J.S. Hale).

[1] Present address: Luxembourg Institute of Science and Medicine, Maison de l'Innovation, 5, Avenue des Haut-Fourneaux, L-4362 Esch-sur-Alzette, Luxembourg.

https://doi.org/10.1016/j.jnnfm.2020.104398
Received 19 March 2020; Received in revised form 28 August 2020; Accepted 9 September 2020
Available online 19 September 2020
0377-0257/© 2020 The Authors. Published by Elsevier B.V. This is an open access article under the CC BY license (http://creativecommons.org/licenses/by/4.0/).

et al. [11,12] that are in turn based on the earlier theoretical work of Rajagopal and Srinivasa [13]. We remark that our work is based on a phenomenological approach to developing viscoelastic models; cf. the popular micromechanical approach, see e.g. Freund et al. [14]. The first model was derived by Málek et al. [11] to describe asphalt binders. The second model can be found in [12], where it is discussed as an equivalent of the classical Burgers model, cf. Burgers [15]. Both models were developed to describe incompressible materials, meaning that all admissible deformations of a body constituted by the given material have to be isochoric. A key differentiating feature between the two models is that the former maintains the instantaneous purely elastic and purely dissipative parts of the total deformation to be isochoric, while the latter admits the instantaneous parts to be compressible (yet the total deformation remains isochoric). The third model is obtained as a combination of the two. This newly proposed phenomenological model describes the material as being composed of different substances, where some of them respond as an incompressible material and some of them as a compressible material.

All of the models we consider have the capability to capture two relaxation mechanisms, although in principle this could be extended further at the expense of introducing extra parameters that need identifying. All variants considered in this study have five parameters, one related to the additional viscous dissipation along with two pairs of parameters (dynamic viscosity and elastic shear modulus) associated with the two relaxation mechanisms. We show that these parameters can be identified using torque and normal force data from a plate–plate rheometer experiment. In the plate–plate configuration each model leads to a coupled system of ordinary differential equation (ODE) that can be solved numerically to compute estimates of the torque and the normal force for a given parameter set, see [12]. For each model the optimal set of parameters is found by minimising the loss between the data and the ODE model in a weighted least-squares sense. An advantage of the chosen approach is that the model is developed directly in a three-dimensional setting allowing parameter identification using experimental data, and/or subsequent direct use of the model and its parameters in numerical simulations of flows in complex geometries discretised using an appropriate numerical method.

The main contributions of this paper are as follows:

- We propose a constitutive model with two relaxation mechanisms that is in turn shown to be superior to two existing models of the same type in predicting the behaviour of SBR in a plate–plate rheometry experiment.
- In contrast with Málek et al. [11], we use a least-squares loss function to define the optimal or best parameter set for each model. Furthermore, we define a procedure for model selection based on choosing the model with minimum loss function at the optimised parameters.
- We demonstrate how a tree-structured Parzen estimator (TPE) algorithm, see Bergstra et al. [16], can be used to find a good initial guess for the parameters. The initial guess is then used in a subsequent Nelder–Mead simplex minimisation algorithm, see Nelder and Mead [17], to find the optimal parameter set.
- We use a Monte-Carlo analysis to show that a relatively low variance in the radius of the sample leads to a large variance in the output torque. This finding confirms comments from experimental papers, e.g. Hellström et al. [18], that it is critical to control the sample radius for repeatability.

An outline of this paper is as follows; in Section 2 we give an overview of the general governing and constitutive equations of a viscoelastic fluid. In Section 3 we derive a system of ODEs describing the flow of a viscoelastic fluid in the plate–plate rheometry configuration. In Section 4 we describe the experimental setup. In Section 5 we explain the procedure for finding the optimal parameter set for each model and selecting the best model. We show the results of our numerical study in Section 6, before concluding with a discussion in Section 7.

2. Mathematical description of viscoelastic fluids

2.1. Governing equations

The kinematics of the isothermal flow of a fluid-like material in a given space–time domain $\Omega \times (0, t_{\mathrm{end}}]$ is mathematically described by the following system of partial differential equations (PDEs), namely

$$\varrho \left(\partial_t \mathbf{v} + (\nabla \mathbf{v})\mathbf{v}\right) = \operatorname{div} \mathbb{T} + \varrho \mathbf{g}, \tag{1a}$$

$$\partial_t \varrho + \operatorname{div}(\varrho \mathbf{v}) = 0. \tag{1b}$$

This system needs to be supplemented by an appropriate set of initial conditions at time $t = 0$ and a set of time-dependent boundary conditions defined on $\partial\Omega \times (0, t_{\mathrm{end}}]$ which we will discuss later.

In the above equations, $\mathbf{v}$ is the velocity, ϱ is the density, $\mathbb{T}$ is the symmetric Cauchy stress tensor and $\mathbf{g}$ is the vector of gravitational acceleration. The gravitational force is assumed to be the only body force acting on the fluid. Introducing the cylindrical coordinate system $\{\mathbf{e}_r, \mathbf{e}_\varphi, \mathbf{e}_z\}$ with the coordinates (r, φ, z), such that $\mathbf{g}$ is aligned with $\mathbf{e}_z$ but pointing in the opposite direction, we may write $\mathbf{g} = -\nabla(gz)$.

In this paper we will limit ourselves to homogeneous, incompressible fluids for which the Cauchy stress tensor $\mathbb{T}$ may be written as

$$\mathbb{T} = -\tilde{p}\mathbb{I} + \mathbb{S}. \tag{2}$$

Here, $\mathbb{I}$ is the unit tensor, $\mathbb{S}$ is the extra stress tensor and $\tilde{p}$ is the pressure. More precisely, $\tilde{p}$ is the Lagrange multiplier that enforces the constraint of incompressibility, see Rajagopal [19]. As such, it must be treated as a primitive variable in the description of the flow. Let p denote the pressure including the hydrostatic contribution in the sense of the definition

$$p \overset{\text{def}}{=} \tilde{p} + \varrho g z. \tag{3}$$

This allows us to rewrite the balance of linear momentum (1a) in the form

$$\varrho \left(\partial_t \mathbf{v} + (\nabla \mathbf{v})\mathbf{v}\right) + \nabla p = \operatorname{div} \mathbb{S}. \tag{4a}$$

Furthermore, due to the assumptions of homogeneity and incompressibility, the balance of mass (1b) reduces to

$$\operatorname{div} \mathbf{v} = 0. \tag{4b}$$

2.2. Constitutive equations

In order to supply the dynamic response of the material into the mathematical model, we need to characterise the extra stress tensor $\mathbb{S}$ by means of a constitutive equation which relates it to the strain history. Before we discuss some specific examples of such relations, let us make a few comments on the notation used in the remainder of the document.

2.2.1. Remarks on notation

The symbols $\mathbb{L}$ and $\mathbb{D}$ are reserved for the velocity gradient and its symmetric part, that is,

$$\mathbb{L} \overset{\text{def}}{=} \nabla \mathbf{v}, \qquad \mathbb{D} \overset{\text{def}}{=} \frac{1}{2}(\mathbb{L} + \mathbb{L}^{\top}). \tag{5}$$

The quantity $\mathbb{D}$ is also known as the rate-of-deformation tensor. Its norm, $|\mathbb{D}| = \sqrt{\mathbb{D} : \mathbb{D}}$, is used to introduce the shear rate $\dot{\gamma}$ through the formula[2]

$$\dot{\gamma} \overset{\text{def}}{=} \sqrt{2}\,|\mathbb{D}|\,. \tag{6}$$

---

[2] The scale factor in the definition (6) ensures conformity with the classical notion of shear rate in the context of the simple shear flow.

The upper convected time derivative of an arbitrary second-order tensor $\mathbb{A}$ is given by

$$\overset{\triangledown}{\mathbb{A}} \overset{\text{def}}{=} \partial_t \mathbb{A} + (\nabla \mathbb{A})\mathbf{v} - \mathbb{L}\mathbb{A} - \mathbb{A}\mathbb{L}^\top, \tag{7}$$

while its deviatoric (traceless) part is defined as

$$\mathbb{A}^\delta \overset{\text{def}}{=} \mathbb{A} - \frac{1}{3}(\operatorname{Tr} \mathbb{A})\mathbb{I}. \tag{8}$$

2.2.2. *Models studied in this work*

We are interested in the specific class of viscoelastic rate-type fluid models that can be derived in a thermodynamically consistent manner using the framework proposed by Rajagopal and Srinivasa [13]. This thermodynamic framework has been further extended and successfully used to develop models for describing the mechanical response of materials as complicated as asphalt binders; see Krishnan and Rajagopal [20] and related papers by Narayan et al. [21,22] or Málek et al. [11,23]. Let us briefly discuss the main ideas of the chosen approach in the following paragraph; consult Málek et al. [12] and the references therein for the detailed explanation.

In general, the observed fluid-like material can be associated with an abstract body which may occupy regions of three-dimensional Euclidean space. The approach by Rajagopal and Srinivasa [13] builds on the assumption of the existence of a natural configuration associated with the placement of a body that evolves as the body deforms, see Fig. 1. This concept allows one to split the total deformation into that associated with the purely elastic response and the dissipative response. Such a decomposition becomes useful when prescribing the way in which the body stores and dissipates energy. This piece of information is supplied into the model by means of two constitutive assumptions specifying the Helmholtz free energy ψ and the rate of entropy production ξ. Depending on the precise form of these two scalar functions, one can obtain different forms of the Cauchy stress tensor $\mathbb{T}$ including its evolution equation.

If the material is known to possess more relaxation mechanisms, typically due to its complex microstructure, then the fundamental idea applied in the derivation of a suitable model is to associate these mechanisms with different underlying natural configurations. The present numerical study compares several models which can be written in the canonical form

$$\mathbb{S} = 2\mu_0 \mathbb{D} + G_1(\mathbb{B}_1 - \mathbb{I}) + G_2(\mathbb{B}_2 - \mathbb{I}), \tag{9a}$$

$$\mu_1 \overset{\triangledown}{\mathbb{B}}_1 = -G_1 \mathcal{Y}_1(\mathbb{B}_1), \tag{9b}$$

$$\mu_2 \overset{\triangledown}{\mathbb{B}}_2 = -G_2 \mathcal{Y}_2(\mathbb{B}_2). \tag{9c}$$

Here, each $\mathbb{B}_n = \mathbb{F}_n \mathbb{F}_n^\top$ $(n \in \{1, 2\})$ denotes the left Cauchy–Green tensor associated with the elastic response between the nth natural configuration and the current configuration of the deformed body, while $\mathcal{Y}_n$ represents a tensor function which takes the respective $\mathbb{B}_n$ as its single argument.[3] Finally, μ_n and G_n are model parameters with the meaning of dynamic viscosity and elastic shear modulus respectively. The term with μ_0 appearing in (9a) describes the additional viscous dissipation.[4] Each of the two relaxation mechanisms, which can be captured by the present class of models, is characterised by the relaxation time λ_n according to the formula

$$\lambda_n \overset{\text{def}}{=} \frac{\mu_n}{G_n}, \quad n \in \{1, 2\}. \tag{10}$$

Table 1 specifies the three models of our interest. Each model is labelled by $\mathcal{M}$ with a pair of subindices indicating either **L**inearity or **N**onlinearity of the functions $\mathcal{Y}_1$ and $\mathcal{Y}_2$ respectively. Table 2 summarises the basic rheometric functions, obtainable in the *simple shear flow* and/or *capillary flow* configurations, for the present models.

Table 1

Variants of viscoelastic models for SBR given by constitutive equations in the form (9).

Model	$\mathcal{Y}_1(\mathbb{B}_1)$	$\mathcal{Y}_2(\mathbb{B}_2)$	Parameters
$\mathcal{M}_{\text{LL}}$	$\mathbb{B}_1 - \mathbb{I}$	$\mathbb{B}_2 - \mathbb{I}$	$m_{\text{LL}} = (\mu_0, \mu_1, \mu_2, G_1, G_2)$
$\mathcal{M}_{\text{NN}}$	$\mathbb{B}_1 \mathbb{B}_1^\delta$	$\mathbb{B}_2 \mathbb{B}_2^\delta$	$m_{\text{NN}} = (\mu_0, \mu_1, \mu_2, G_1, G_2)$
$\mathcal{M}_{\text{LN}}$	$\mathbb{B}_1 - \mathbb{I}$	$\mathbb{B}_2 \mathbb{B}_2^\delta$	$m_{\text{LN}} = (\mu_0, \mu_1, \mu_2, G_1, G_2)$

Table 2

Expressions representing the shear viscosity η and the normal stress differences N_1, N_2 derived from models in Table 1. Models $\mathcal{M}_{\text{NN}}$ and $\mathcal{M}_{\text{LN}}$ capture shear thinning, model $\mathcal{M}_{\text{LL}}$ does not.

Model	$\eta(\dot\gamma)$	$N_1(\dot\gamma)$	$N_2(\dot\gamma)$
$\mathcal{M}_{\text{LL}}$	$\mu_1 + \mu_2$	$2(\mu_1\lambda_1 + \mu_2\lambda_2)\dot\gamma^2$	0
$\mathcal{M}_{\text{NN}}$	$\mu_0 + \mu_1 A_1 + \mu_2 A_2$	$2(\mu_1\lambda_1 A_1^{3/2} + \mu_2\lambda_2 A_2^{3/2})\dot\gamma^2$	$-(\mu_1\lambda_1 A_1^{3/2} + \mu_2\lambda_2 A_2^{3/2})\dot\gamma^2$
$\mathcal{M}_{\text{LN}}$	$\mu_0 + \mu_1 + \mu_2 A_2$	$2(\mu_1\lambda_1 + \mu_2\lambda_2 A_2^{3/2})\dot\gamma^2$	$-\mu_2\lambda_2 A_2^{3/2}\dot\gamma^2$

Notation: $A_n = \frac{\sqrt{1+4(\lambda_n\dot\gamma)^2}-1}{2(\lambda_n\dot\gamma)^2}$ for $n \in \{1, 2\}$.

The first model ($\mathcal{M}_{\text{LL}}$) is formally equivalent to the classical Burgers model, see [12]. The second model ($\mathcal{M}_{\text{NN}}$) was previously used to describe the response of asphalt binders, see [11]. Both models describe incompressible fluids in the sense that the total deformation remains isochoric. The difference between them is given by the fact that the instantaneous purely elastic and purely dissipative parts of the total deformation – associated with individual natural configurations – are not necessarily isochoric in the first case ($\mathcal{M}_{\text{LL}}$), but the opposite holds true in the second case ($\mathcal{M}_{\text{NN}}$). The third model ($\mathcal{M}_{\text{LN}}$) is a combination of both.

To best of our knowledge, the last model has not been explicitly considered within the context of modelling the response of materials such as SBR. That said, let us emphasise that all variants covered in the present work are special cases of general multi-mode viscoelastic models with their individual modes corresponding to simpler, well established models (see Remark 2.1). There are multiple ways to derive such multi-mode models. The basic ideas for a unified derivation of the variants from Table 1 within the framework discussed above are presented in Section 2.3 for the specific case $\mathcal{M}_{\text{LN}}$.

Remark 2.1. Constitutive equations in the canonical form (9) represent a general multi-mode viscoelastic model limited to the case with two modes and a separate viscous contribution. The linear mode L corresponds to the well-known upper convected Maxwell (UCM) model or, more precisely, to the classical Oldroyd-B model taking into account the separate viscous contribution; see Oldroyd [24]. On the other hand, the nonlinear mode N can be recognised as the simplest Leonov model; see Leonov [25]. Indeed, if we formally disable the linear mode (and the separate viscous contribution) in the combined model $\mathcal{M}_{\text{LN}}$, we will end up with the single-mode model

$$\mathbb{S} = G(\mathbb{B} - \mathbb{I}), \tag{11a}$$

$$\mu \overset{\triangledown}{\mathbb{B}} = -G \mathbb{B}\mathbb{B}^\delta, \tag{11b}$$

where we have omitted the superfluous subscripts.[5] The above equations represent the Leonov model for a Maxwellian isotropic viscous medium; see [25, Section 3.1]. Further discussion regarding the Leonov model and its variants can be found e.g. in [26, Section 8.1.3-C].

---

[3] Note that the two Eqs. (9b) and (9c) are coupled through the velocity field and its gradient in the objective part of the time derivative (7).

[4] The idea to incorporate the additional dissipation term into the models considered in this work is motivated by the experimental observations discussed further in Section 4.2.

[5] We should write $\mathbb{B}_{\kappa_{p(t)}}$ instead of $\mathbb{B}$ to emphasise the fact that this quantity characterises the deformation experienced by the "spring" part of the virtual spring-dashpot system shown in Fig. 1.

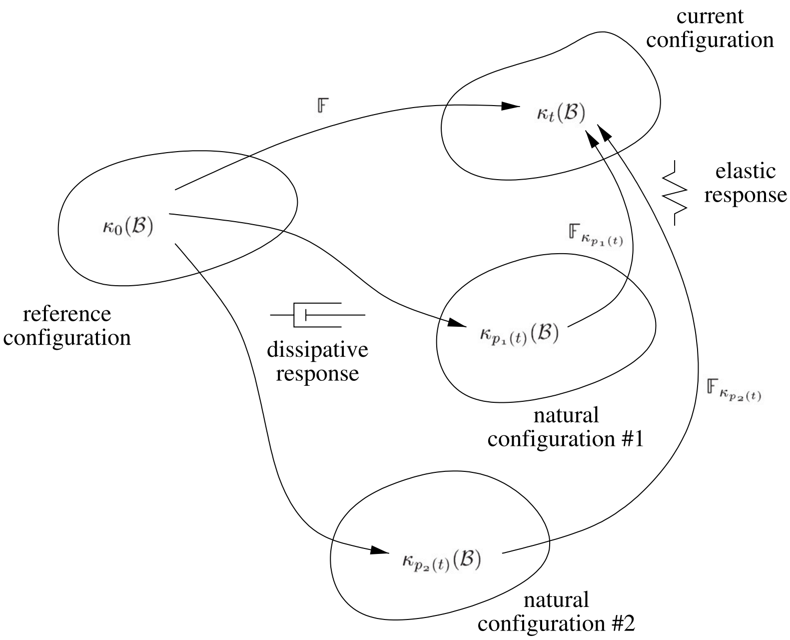

Fig. 1. Using two natural configurations, $\kappa_{p_1(t)}$ and $\kappa_{p_2(t)}$, the total deformation $\mathbb{F}$ is split into dissipative parts and purely elastic parts corresponding to the mappings $\mathbb{F}_{\kappa_{p_1(t)}} \equiv \mathbb{F}_1$ and $\mathbb{F}_{\kappa_{p_2(t)}} \equiv \mathbb{F}_2$.

2.3. Derivation of the model $\mathcal{M}_{\mathrm{LN}}$

Recall that the Eqs. (1a) and (1b) describe the balance of mass and the balance of linear momentum for the given physical system. The balance of angular momentum is in our case equivalent to the requirement that the Cauchy stress tensor $\mathbb{T}$ is symmetric. Let us rewrite this basic set of balance equations in the form

$$\dot{\varrho} = -\varrho \operatorname{div} \mathbf{v}, \tag{12a}$$

$$\varrho \dot{\mathbf{v}} = \operatorname{div} \mathbb{T} + \varrho \mathbf{g} \quad \text{with} \quad \mathbb{T} = \mathbb{T}^\top, \tag{12b}$$

where $\dot{z} \overset{\text{def}}{=} \partial_t z + \mathbf{v} \cdot \nabla z$ is the shorthand notation for the material time derivative, which is used exclusively within this section. Following the framework outlined in [12, Section 2.2], we consider the additional equation

$$\xi = \mathbb{T} : \mathbb{D} - \varrho \dot{\psi} \quad \text{with} \quad \xi \geq 0, \tag{13}$$

which can be obtained – under circumstances where only isothermal processes are allowed – by combining the balance of energy and the formulation of the second law of thermodynamics.

As the material is supposed to be incompressible, it can undergo only isochoric motions, meaning that $\operatorname{Tr} \mathbb{D} = \operatorname{div} \mathbf{v} = 0$. With this constraint the balance of mass reduces to

$$\dot{\varrho} = 0. \tag{14}$$

Next, we assume that

$$\psi = \psi_0(\varrho) + \frac{G_1}{2\varrho}\left(\operatorname{Tr} \mathbb{B}_1 - 3 - \ln\left(\det \mathbb{B}_1\right)\right) + \frac{G_2}{2\varrho}\left(\operatorname{Tr} \mathbb{B}_2 - 3\right), \tag{15}$$

which is the formula that describes the way in which the material stores the energy. It says that the elastic response from the first natural configuration corresponds to that of compressible neo-Hookean solid, while the response from the second one is the same but incompressible. Inserting (15) into (13), using also (14) and doing some further algebraic manipulations[6] (see [27, Section 4.4.1]), we end up with

$$\xi = (\mathbb{T} - G_1\mathbb{B}_1 - G_2\mathbb{B}_2) : \mathbb{D} + G_1(\mathbb{C}_1 - \mathbb{I}) : \mathbb{D}_1 + G_2\mathbb{C}_2 : \mathbb{D}_2, \tag{16}$$

where $\mathbb{C}_n = \mathbb{F}_n^\top \mathbb{F}_n$ $(n \in 1, 2)$ denotes the right Cauchy–Green tensor associated with the elastic part of the total deformation (with respect to the nth natural configuration) and $\mathbb{D}_n$ is defined by means of its complementary irreversible part $\mathbb{G}_n = \mathbb{F}_n^{-1}\mathbb{F}$, where $\mathbb{F}$ denotes the total deformation gradient, see [27, Eq. (157)–(158)]. The dissipative mechanism associated with the viscous response from the second natural configuration is assumed to be that for an incompressible fluid, meaning that $\operatorname{Tr} \mathbb{D}_2 = 0$.

Using the incompressibility constraints $\operatorname{Tr} \mathbb{D} = \operatorname{Tr} \mathbb{D}_2 = 0$, and the decompositions (2) and (8), we rewrite the expression (16) to take the form

$$\xi = (\mathbb{S}^\delta - G_1\mathbb{B}_1^\delta - G_2\mathbb{B}_2^\delta) : \mathbb{D}^\delta + G_1(\mathbb{C}_1 - \mathbb{I}) : \mathbb{D}_1 + G_2\mathbb{C}_2^\delta : \mathbb{D}_2^\delta. \tag{17}$$

As a next step we postulate that

$$\mathbb{S}^\delta - G_1\mathbb{B}_1^\delta - G_2\mathbb{B}_2^\delta = 2\mu_0\mathbb{D}^\delta, \tag{18a}$$

$$G_1(\mathbb{C}_1 - \mathbb{I}) = 2\mu_1\mathbb{D}_1\mathbb{C}_1, \tag{18b}$$

$$G_2\mathbb{C}_2^\delta = 2\mu_2\mathbb{D}_2^\delta. \tag{18c}$$

These constitutive relations ensure that $\xi = 2\mu_0\left|\mathbb{D}^\delta\right|^2 + 2\mu_1\left|\mathbb{F}_1\mathbb{D}_1\right|^2 + 2\mu_2\left|\mathbb{D}_2^\delta\right|^2 \geq 0$. Each of the last two relations can be rewritten in terms of the corresponding $\mathbb{B}_n = \mathbb{F}_n\mathbb{F}_n^\top$ using the identity

$$\overset{\triangledown}{\mathbb{B}}_n = -2\mathbb{F}_n\mathbb{D}_n\mathbb{F}_n^\top, \quad n \in \{1, 2\}, \tag{19}$$

see [27, Eq. (163)]. We proceed as follows. First, multiplying (18b) from the left by $\mathbb{F}_1$ and from the right by $\mathbb{F}_1^{-1}$ we obtain

$$G_1(\mathbb{B}_1 - \mathbb{I}) = 2\mu_1\mathbb{F}_1\mathbb{D}_1\mathbb{F}_1^\top. \tag{20}$$

Second, multiplying (18c) from the left by $\mathbb{F}_2$ and from the right by $\mathbb{F}_2^\top$, and recalling $\operatorname{Tr} \mathbb{C}_2 = \operatorname{Tr} \mathbb{B}_2$, we obtain

$$G_2\left(\mathbb{B}_2^2 - \frac{1}{3}\left(\operatorname{Tr} \mathbb{B}_2\right)\mathbb{B}_2\right) = 2\mu_2\mathbb{F}_2\mathbb{D}_2\mathbb{F}_2^\top. \tag{21}$$

Finally, we use (19) to replace the tensor product on the right hand side in the above relations by the upper convected time derivative of the corresponding left Cauchy–Green tensor. After some additional algebraic manipulations, we rewrite the constitutive relations (18) to

---

[6] In particular, we make use of the identities $\dot{\overline{\operatorname{Tr} \mathbb{B}_n}} = 2\mathbb{B}_n : \mathbb{D} - 2\mathbb{C}_n : \mathbb{D}_n$ and $\dot{\overline{\ln\left(\det \mathbb{B}_n\right)}} = 2\mathbb{I} : \mathbb{D} - 2\mathbb{I} : \mathbb{D}_n$.

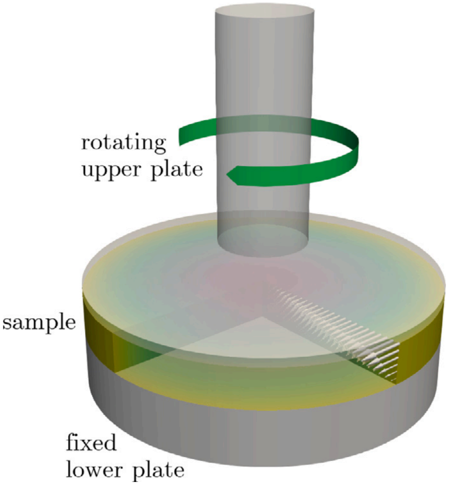

Fig. 2. Sketch of the rotational plate–plate rheometer.

take their final form

$$\mathbb{S} = -\phi\mathbb{I} + 2\mu_0\mathbb{D} + G_1(\mathbb{B}_1 - \mathbb{I}) + G_2(\mathbb{B}_2 - \mathbb{I}), \tag{22a}$$

$$\mu_1 \overset{\triangledown}{\mathbb{B}}_1 = -G_1(\mathbb{B}_1 - \mathbb{I}), \tag{22b}$$

$$\mu_2 \overset{\triangledown}{\mathbb{B}}_2 = -G_2\mathbb{B}_2\mathbb{B}_2^{\delta}, \tag{22c}$$

with the term $\phi \overset{\text{def}}{=} -(\frac{1}{3}\operatorname{Tr}\mathbb{S} + G_1 - \frac{1}{3}G_1\operatorname{Tr}\mathbb{B}_1 + G_2 - \frac{1}{3}G_2\operatorname{Tr}\mathbb{B}_2)$ that can be incorporated into the pressure variable p similarly as the hydrostatic contribution in the definition (3).

3. Plate–plate rheometry

A rotational shear flow is examined in the plate–plate geometry for the constitutive equations discussed previously in Section 2.2. In this configuration, a sample of a fluid-like material is placed between two cylindrical plates, where the lower one is fixed and the upper one can rotate around its axis, see Fig. 2. The diameter of the sample, $D = 2R$, is supposed to coincide with the diameter of the plates. The fixed distance between the plates is denoted by H. The material is assumed to stick to the plates, and the flow induced by the rotation is considered to be laminar and axisymmetric.

We shall focus on the experimental setting with the controlled shear rate, that is, with the controlled rotational speed. We suppose that the material flows only in the azimuthal direction $\mathbf{e}_{\varphi}$, satisfying the no-slip boundary condition at the plates, and the no-traction condition applies on the lateral surface which remains vertical during the deformation. More precisely, we put

$$\mathbf{v} = \frac{rz\omega}{H}\mathbf{e}_{\varphi}, \qquad \omega \geq 0, \tag{23}$$

where ω denotes the angular velocity that is controlled in time, see (43). The above *ansatz* satisfies (4b) and further implies

$$\begin{aligned} \mathbb{L} &= \frac{r\omega}{H}\mathbf{e}_{\varphi}\otimes\mathbf{e}_z + \frac{z\omega}{H}\left(\mathbf{e}_{\varphi}\otimes\mathbf{e}_r - \mathbf{e}_r\otimes\mathbf{e}_{\varphi}\right), \\ \mathbb{D} &= \frac{r\omega}{2H}\left(\mathbf{e}_{\varphi}\otimes\mathbf{e}_z + \mathbf{e}_z\otimes\mathbf{e}_{\varphi}\right). \end{aligned} \tag{24}$$

Then, according to (6), we have

$$\dot{\gamma} = \frac{r\omega}{H}. \tag{25}$$

The corresponding strain γ can be obtained by integrating the previous relation in time. In this way, one obtains

$$\gamma = \frac{r\Theta}{H}, \tag{26}$$

where Θ denotes the amount of rotation of the upper plate in the sense of the relation $\omega = \mathrm{d}_t\Theta$.

Supposing that we are dealing with the creeping flow, so that the inertial effects can be neglected, the balance of linear momentum reads

$$\partial_r S_{rr} + \partial_z S_{rz} + \frac{1}{r}(S_{rr} - S_{\varphi\varphi}) = \partial_r p, \tag{27a}$$

$$\partial_r S_{r\varphi} + \partial_z S_{\varphi z} + \frac{2}{r}S_{r\varphi} = 0, \tag{27b}$$

$$\partial_r S_{rz} + \partial_z S_{zz} + \frac{1}{r}S_{rz} = \partial_z p. \tag{27c}$$

These equations are further coupled with constitutive equations in the form (9). In particular, the components of $\mathbb{B}_n$ ($n \in \{1,2\}$) must satisfy the system of evolution equations (28a)–(28f) given in Box I.

Let us emphasise that none of these equations explicitly depends on the variable z. We shall assume that the material is initially at rest and relaxed, meaning that

$$\mathbb{S}_n\big|_{t=0} = \mathbb{O}, \qquad \mathbb{B}_n\big|_{t=0} = \mathbb{I}, \qquad n \in \{1,2\}, \tag{29}$$

where $\mathbb{O}$ denotes the zero tensor. Since the initial conditions do not depend on z, it follows from (28) that the same must hold for the components of $\mathbb{B}_n$ (for $t > 0$) regardless of the choice of $\mathcal{Y}_n$. As a consequence, the components of $\mathbb{S}$ are also independent of z, see (9a) and (24). Moreover, the choice of initial conditions in (29) ensures that $B_{n|r\varphi} = B_{n|rz} = 0$, see (28e) and (28f), and thus also $S_{r\varphi} = S_{rz} = 0$. Based on these observations, we see that the left hand side of (27c) is identically equal to zero, so that p is independent of z, (27b) is identically satisfied and (27a) can be rewritten as[7]

$$\mathrm{d}_r T_{rr} + \frac{1}{r}(T_{rr} - T_{\varphi\varphi}) = 0. \tag{30}$$

We are interested in computing the torque M and the normal force F on the upper plate $\Gamma_U \subset \partial\Omega$. These quantities are defined by

$$M(t;\mathcal{M},m) \overset{\text{def}}{=} \int_{\Gamma_U} rT_{\varphi z}\,\mathrm{d}s = 2\pi\int_0^R r^2 S_{\varphi z}\,\mathrm{d}r, \tag{31}$$

$$F(t;\mathcal{M},m) \overset{\text{def}}{=} \int_{\Gamma_U} T_{zz}\,\mathrm{d}s = 2\pi\int_0^R r(S_{zz} - \tilde{p})\,\mathrm{d}r, \tag{32}$$

where we have explicitly denoted the dependence of the computed torque and normal force on time, but also on the choice of model $\mathcal{M} \in \left\{\mathcal{M}_{\mathrm{LL}}, \mathcal{M}_{\mathrm{NN}}, \mathcal{M}_{\mathrm{LN}}\right\}$ and the corresponding parameter set $m \in \left\{m_{\mathrm{LL}}, m_{\mathrm{NN}}, m_{\mathrm{LN}}\right\}$.

The expression for the computation of the normal force can be rewritten in terms of normal stress differences using Eq. (30), see [11]. The alternative formula reads

$$F(t;\mathcal{M},m) = \pi\int_0^R r(S_{rr} - S_{\varphi\varphi})\,\mathrm{d}r + 2\pi\int_0^R r(S_{zz} - S_{rr})\,\mathrm{d}r. \tag{33}$$

The integrals in (31) and (33) are computed using a three-point Newton–Cotes quadrature scheme (Simpson's rule). At each quadrature point the system of ODEs (28) is solved using a fourth-order adaptive Runge–Kutta method. We implement the solver using the routines available in the Python library SciPy, see Jones et al. [28].

4. Experimental setup

4.1. Sample preparation

The sample under investigation is SBR containing 27% of styrene with functionalised chain-ends that are designed to enhance the interaction with silica fillers. The SBR has a molecular weight of 310 000 g mol^{-1} measured with gel permeation chromatography (GPC) relative to polystyrene standard. The samples under investigation do

---

[7] Recall the decomposition (2) and use the fact that $\partial_r p = \partial_r \tilde{p}$ according to (3).

$$\partial_t B_{n|rr} = - \frac{G_n}{\mu_n} \begin{cases} B_{n|rr} - 1 & [\text{if } \mathcal{Y}_n(\mathbb{B}_n) = \mathbb{B}_n - \mathbb{I}], \\ (B^2_{n|rr} + B^2_{n|r\varphi} + B^2_{n|rz} - \frac{1}{3} B_{rr} \operatorname{Tr} \mathbb{B}_n) & [\text{if } \mathcal{Y}_n(\mathbb{B}_n) = \mathbb{B}_n \mathbb{B}^{\delta}_n], \end{cases} \tag{28a}$$

$$\partial_t B_{n|\varphi\varphi} = 2 \frac{r\omega}{H} B_{n|\varphi z} - \frac{G_n}{\mu_n} \begin{cases} B_{n|\varphi\varphi} - 1 & [\text{if } \mathcal{Y}_n(\mathbb{B}_n) = \mathbb{B}_n - \mathbb{I}], \\ (B^2_{n|r\varphi} + B^2_{n|\varphi\varphi} + B^2_{n|\varphi z} - \frac{1}{3} B_{\varphi\varphi} \operatorname{Tr} \mathbb{B}_n) & [\text{if } \mathcal{Y}_n(\mathbb{B}_n) = \mathbb{B}_n \mathbb{B}^{\delta}_n], \end{cases} \tag{28b}$$

$$\partial_t B_{n|zz} = - \frac{G_n}{\mu_n} \begin{cases} B_{n|zz} - 1 & [\text{if } \mathcal{Y}_n(\mathbb{B}_n) = \mathbb{B}_n - \mathbb{I}], \\ (B^2_{n|rz} + B^2_{n|\varphi z} + B^2_{n|zz} - \frac{1}{3} B_{zz} \operatorname{Tr} \mathbb{B}_n) & [\text{if } \mathcal{Y}_n(\mathbb{B}_n) = \mathbb{B}_n \mathbb{B}^{\delta}_n], \end{cases} \tag{28c}$$

$$\partial_t B_{n|\varphi z} = \frac{r\omega}{H} B_{n|zz} - \frac{G_n}{\mu_n} \begin{cases} B_{n|\varphi z} & [\text{if } \mathcal{Y}_n(\mathbb{B}_n) = \mathbb{B}_n - \mathbb{I}], \\ B_{n|\varphi z}(B_{n|\varphi\varphi} + B_{n|zz} - \frac{1}{3} \operatorname{Tr} \mathbb{B}_n) + B_{n|r\varphi} B_{n|rz} & [\text{if } \mathcal{Y}_n(\mathbb{B}_n) = \mathbb{B}_n \mathbb{B}^{\delta}_n], \end{cases} \tag{28d}$$

$$\partial_t B_{n|r\varphi} = \frac{r\omega}{H} B_{n|rz} - \frac{G_n}{\mu_n} \begin{cases} B_{n|r\varphi} & [\text{if } \mathcal{Y}_n(\mathbb{B}_n) = \mathbb{B}_n - \mathbb{I}], \\ B_{n|r\varphi}(B_{n|rr} + B_{n|\varphi\varphi} - \frac{1}{3} \operatorname{Tr} \mathbb{B}_n) + B_{n|rz} B_{n|\varphi z} & [\text{if } \mathcal{Y}_n(\mathbb{B}_n) = \mathbb{B}_n \mathbb{B}^{\delta}_n], \end{cases} \tag{28e}$$

$$\partial_t B_{n|rz} = - \frac{G_n}{\mu_n} \begin{cases} B_{n|rz} & [\text{if } \mathcal{Y}_n(\mathbb{B}_n) = \mathbb{B}_n - \mathbb{I}], \\ B_{n|rz} \left(B_{n|rr} + B_{n|zz} - \frac{1}{3} \operatorname{Tr} \mathbb{B}_n \right) + B_{n|r\varphi} B_{n|\varphi z} & [\text{if } \mathcal{Y}_n(\mathbb{B}_n) = \mathbb{B}_n \mathbb{B}^{\delta}_n]. \end{cases} \tag{28f}$$

Box I.

not contain any fillers (e.g. silica, carbon black) or curatives. However, some other ingredients are incorporated to improve the processability, see Gansen et al. [29] for more details. After mixing and milling, the rubber has the form of a large rubber sheet of an approximate thickness of 4 mm with a highly corrugated surface (Fig. 3(a)). From this sheet, two discs with a diameter of 20 mm are stamped out. These two discs are positioned one above the other and placed between the two plates of the Haake Mars plate–plate rheometer. A sealed oven encloses the sample. The oven is heated up to 120 °C and the sample is slowly compressed to a thickness of around 5 mm. This procedure typically takes between one and two hours. After cooling down the sample to room temperature, it is carefully removed and due to the compression the excess rubber is removed by stamping the sample out again (Fig. 3(b)).

4.2. Experimental procedure

A modified stress relaxation test is conducted to produce experimental data. The standard stress relaxation test requires the application of a step increase in strain, which is afterwards held constant for a given time. The stress that builds up inside the material, as a consequence of its sudden deformation, will relax over time due to various molecular mechanisms. In the torsional configuration described in Section 3, the application of the step strain corresponds to the instantaneous change of the deflection angle Θ, see (26). It is of course physically impossible to twist the sample instantly. The reason is twofold. First, the equipment ramps to the required steady state in a finite time. Second, even if we admit an "instantaneous" deformation to be a fast motion occurring on a time scale that is much shorter than the time of observation, it is not feasible to conduct the experiment under the simplifying conditions discussed in Section 3. Therefore, we tried to use a different testing scheme where the ramping of the deflection angle is controlled to gradually increase to the specified value at $t = t_0$ ($0 < t_0 < t_{\mathrm{end}}$).

To study the stress relaxation of asphalts, Narayan et al. [30] suggested to use the template with the controlled shear rate in terms of the angular velocity of the form

$$\omega(t) = \begin{cases} \omega_0, & t \le t_0, \\ 0, & t > t_0, \end{cases} \tag{34}$$

see (25). Here, ω_0 is a specified constant value. The Haake Mars plate–plate rheometer allows one to set up the required shear rate $\dot{\gamma}_0 = \omega_0 H/R$.

4.3. Experimental data

The experiment was performed at a fixed temperature of 120 °C. Figs. 4–5 show the experimental input/output data for four measurements {A1, A2, B1, B2}. Different samples were used for measurements labelled by different letters. Each of these measurements was repeated twice with the given sample. The thickness of the sample was slightly different in each case as a result of the complicated preparation stage, see Section 4.1. In particular, the mean thickness was $H = 4.82$ mm with the standard deviation of approximately 0.02 mm. The shear rate $\dot{\gamma}_0 = 0.03\ \mathrm{s}^{-1}$ was specified for $t \in (0, t_0]$ with $t_0 = 100$ s. After that, the upper plate was held at the same position and the relaxation of the sample was measured over the additional time of 300 s. The normal force and the torque were recorded simultaneously.

Looking carefully at Fig. 4, we see that the ramping of the deflection angle is not linear during the time interval $(0, t_0]$, meaning that the angular velocity is not constant as we have required. We believe that this behaviour is caused by the complex material properties already discussed above, which make it technically difficult to set up and maintain the specified shear rate. Nevertheless, the ramping was done in a repeated path in most cases. It thus makes sense to take such data, fit it by a customised function ω and use it as an input for the numerical simulation; see relations (41)–(43) in Section 6.

The output data are expected to overlap to a certain extent, taking into account the measurement error as well as the experimental error including variations in the input data for individual measurements (see Fig. 6). The accuracy of the equipment for measuring the torque and the normal force was estimated to be 0.05 mN m and 0.03 N, respectively, following methods suggested by Narayan et al. [30]. In Fig. 5, we see that the measured normal force is almost perfectly consistent in the previous sense. However, a kind of inconsistency is observed in the measured torque for the two different samples. We believe that the observed behaviour is related with the fact that it has not been possible to prepare the two samples with exactly the same radius (with the precision of 0.1 mm). Our conjecture is supported by the numerical experiment in Section 6.2, where we study a sensitivity of the numerical result on the radius of the sample.

a) Before preparation.

b) After preparation.

Fig. 3. SBR sample before preparation as a rubber sheet with dimensions of ∼100 mm × 120 mm, and after preparation as a disc with the diameter of ∼20 mm.

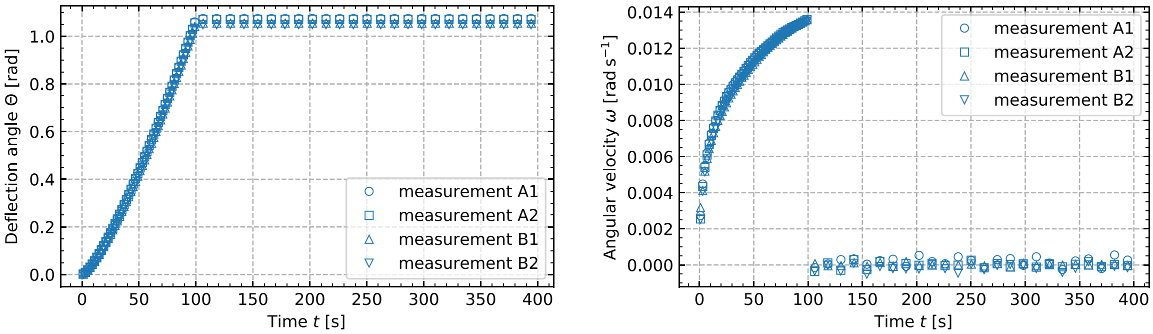

Fig. 4. Experimental input data.

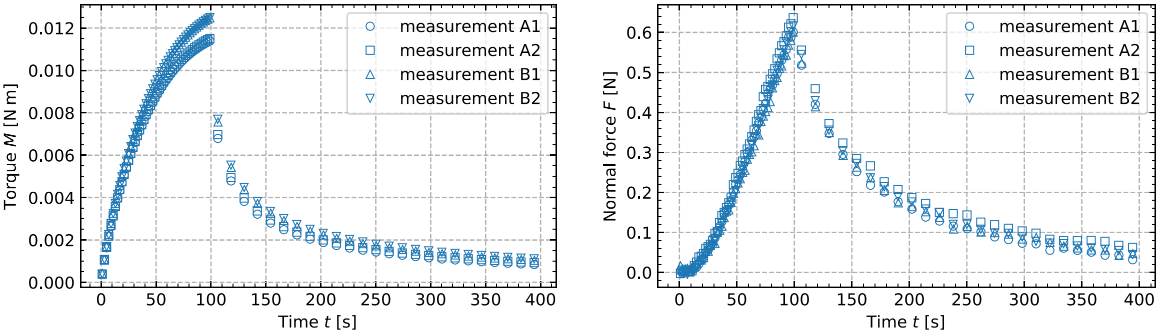

Fig. 5. Experimental output data.

5. The optimisation procedure

Our primary objective is to fit the parameters of the three viscoelastic models proposed in Table 1, using the experimental data produced by the plate–plate rheometer described in Section 4.

The observed experimental data consists of N sets of K discrete torque and normal force measurements, that is, $M^n_{\text{obs}} = (M^n_1, M^n_2, \dots, M^n_K)$ and $F^n_{\text{obs}} = (F^n_1, F^n_2, \dots, F^n_K)$ for $n = 1, 2, \dots, N$. These discrete observations are taken at times $t^n_{\text{obs}} = (t^n_1, t^n_2, \dots, t^n_K)$. We further define an observation operator $\mathcal{G}^n_{\text{obs}} : X \to \mathbb{R}^K$ that takes a function in some function space X and evaluates it at t^n_{obs}. In particular, for $f \in X$ we define

$$\mathcal{G}^n_{\text{obs}} f \overset{\text{def}}{=} \left(f|_{t=t^n_1}, f|_{t=t^n_2}, \dots, f|_{t=t^n_K} \right). \tag{35}$$

With this notation in hand we can define the following cost functional

$$J(\mathcal{M}, m) = \sum_{n=1}^{N} \left(\frac{2}{\Sigma^n_M} \left\| \mathcal{G}^n_{\text{obs}} M(t; \mathcal{M}, m) - M^n_{\text{obs}} \right\|_2 + \frac{1}{\Sigma^n_F} \left\| \mathcal{G}^n_{\text{obs}} F(t; \mathcal{M}, m) - F^n_{\text{obs}} \right\|_2 \right), \tag{36}$$

where $m \in \mathbb{R}^P$ is the generalised set of constitutive parameters for a specific constitutive model $\mathcal{M}$, and $\|\cdot\|_2$ denotes the standard ℓ^2 norm. $M(t; \mathcal{M}, m)$ and $F(t; \mathcal{M}, m)$ are the torque and normal force functions computed by numerical solution of (31) and (33) for a specified m and model $\mathcal{M}$. Let us emphasise that the numerical solution depends on several other parameters, including H, R and ω, which may vary from case to case. The coefficients Σ_M^n and Σ_F^n, defined by

$$\Sigma_M^n \overset{\text{def}}{=} \left\| M_{\text{obs}}^n \right\|_2, \qquad \Sigma_F^n \overset{\text{def}}{=} \left\| F_{\text{obs}}^n \right\|_2, \tag{37}$$

ensure that approximately equal weighting is given to fitting the torque and normal force measurements. However, by considering the multiplication factor 2 in the first term on the right hand side of (36), we give some additional preference to fitting the torque measurements.

Remark 5.1. A slightly different cost functional was used by Málek et al. [11, Eq. (66)] to fit the data for asphalt binders. In particular, the authors have considered

$$J(\mathcal{M}, m) = \frac{1}{K} \sum_{n=1}^{N} \left(\frac{1}{\Sigma_M^n} \left\| \mathcal{G}_{\text{obs}}^n M(t; \mathcal{M}, m) - M_{\text{obs}}^n \right\|_1 + \frac{1}{\Sigma_F^n} \left\| \mathcal{G}_{\text{obs}}^n F(t; \mathcal{M}, m) - F_{\text{obs}}^n \right\|_1 \right),$$

with the weighting coefficients

$$\Sigma_M^n \overset{\text{def}}{=} \left\| M_{\text{obs}}^n \right\|_\infty, \qquad \Sigma_F^n \overset{\text{def}}{=} \left\| F_{\text{obs}}^n \right\|_\infty.$$

Here, $\|\cdot\|_1$ and $\|\cdot\|_\infty$ denote the standard ℓ^1 and ℓ^∞ norms, respectively.

The best set of constitutive parameters for each model $\mathcal{M}$ is then defined as the argument $m \in \mathbb{R}^P$ that minimises (36), namely

$$m_{\text{label}}^* = \operatorname*{arg\,min}_{m \in \mathbb{R}^P} J(\mathcal{M}_{\text{label}}, m) \quad \forall \text{ label} \in \{\text{LL}, \text{NN}, \text{LN}\}. \tag{38}$$

The output of the above process are three sets of optimal parameters $\left\{m_{\text{LL}}^*, m_{\text{NN}}^*, m_{\text{LN}}^*\right\}$ associated with the models $\left\{\mathcal{M}_{\text{LL}}, \mathcal{M}_{\text{NN}}, \mathcal{M}_{\text{LN}}\right\}$, respectively.

Remark 5.2. Since $\dim(m) = P \ll 2KN$, the minimisation problem (38) is overconstrained by the experimental data. Hence, no regularisation term such as Tikhonov (e.g. [31]) or Bayesian (see e.g. [32,33]) is needed. However, the problem is in general non-convex and multiple local minima may exist.

Finally, we define the optimal model $\mathcal{M}^*$ as the model with the lowest value of the functional $J(\mathcal{M}, m)$ evaluated at the associated optimal parameter m^*, that is,

$$\mathcal{M}^* = \operatorname*{arg\,min}_{(\mathcal{M}, m^*) \in \left\{(\mathcal{M}_{\text{LL}}, m_{\text{LL}}^*), (\mathcal{M}_{\text{NN}}, m_{\text{NN}}^*), (\mathcal{M}_{\text{LN}}, m_{\text{LN}}^*)\right\}} J(\mathcal{M}, m^*). \tag{39}$$

Remark 5.3. Because the three models have roughly comparable complexity, involving five parameters and the solution of a similar system of ODEs, we do not penalise model complexity in (39).

The minimisation (38) of the functional (36) is performed in two stages. Because of the presence of multiple local minima of J, we first use the TPE algorithm as a global optimiser to efficiently search across a large subspace of the whole parameter space. The TPE algorithm requires the specification of a joint prior probability density function on the parameters. In a Bayesian context this prior reflects the analyst's belief about the parameters prior to the optimisation. We choose the variables to be independent and with uniform prior spanning two orders of magnitude $\mu_1, \mu_2 \sim \mathcal{U}(10^4, 10^6)$ and $G_1, G_2 \sim \mathcal{U}(10^2, 10^4)$, where $\mathcal{U}(a, b)$ is a uniform random distribution with lower and upper bounds a and b. This corresponds to a weakly informative prior. We use the same prior for all models. We note that our prior does not give preference to a particular ordering of the two relaxation timescales in the proposed $\mathcal{M}_{\text{LN}}$ model.

The output of the TPE algorithm is then denoted $m^{(0)}$ and is subsequently used as an initial guess for a restarted Nelder–Mead algorithm, see [17,34]. The purpose of this second step is to improve the estimate of the local minima in the neighbourhood of $m^{(0)}$. In addition, as suggested by Málek et al. [11], in order to eliminate any further chances of finding local minima, we use the Nelder–Mead algorithm in a restarted fashion in the following sense:

1. we find a solution, that is, a seemingly optimal set of model parameters $m^{(k)}$ using Nelder–Mead,
2. we round the values of $m^{(k)}$ and use them as the new initial guess to find $m^{(k+1)}$.

We repeat the previous steps for $k = 0, 1, \ldots$ until the relative reduction in the functional satisfies

$$\frac{J(\mathcal{M}, m^{(k+1)}) - J(\mathcal{M}, m^{(k)})}{J(\mathcal{M}, m^{(k)})} \leq 10^{-6}. \tag{40}$$

We have found the above two-stage method (TPE followed by Nelder–Mead) to be highly robust in finding a 'reasonable' minimum m^*. The TPE algorithm does not require the user to input a specific initial guess and is reliable in finding a $m^{(0)}$ where the Nelder–Mead algorithm can then work effectively. We use the implementation of TPE found in the Python library Hyperopt, see Bergstra et al. [16], and the Nelder–Mead algorithm from the Python library SciPy.

6. Results

We use the following formula with four constant parameters $\{a, b, c, d\}$ to fit[8] the experimental deflection angle in the first time segment (see Fig. 4), namely

$$\Theta_{\text{fit}}(t) = ab \ln\left(\frac{b}{b+t}\right) + \frac{c}{2}t^2 + (a+d)t, \quad t \in (0, t_0]. \tag{41}$$

The change of the angle in the whole time domain is then captured by the piecewise defined function

$$\Theta(t) = \begin{cases} \Theta_{\text{fit}}(t), & t \leq t_0, \\ \Theta_{\text{fit}}(t_0), & t > t_0, \end{cases} \tag{42}$$

with $t_0 \approx 100$ s. The corresponding change of the angular velocity, which is the *input datum for simulations*, is then given in the form of the discontinuous function

$$\omega(t) = \begin{cases} \frac{at}{b+t} + ct + d, & t \leq t_0, \\ 0, & t > t_0, \end{cases} \tag{43}$$

where the formula for the first time segment is obtained as the time derivative of Θ_{fit}.

Remark 6.1. The reason why we fit the deflection angle data is due to the fact that the rheometer has a sensor for recording the angular displacement of the upper plate. These data are thus expected to be more precise than the angular velocity data, especially at low rotational speeds. This is clearly visible when we explore the data in Fig. 4 for $t > 100$ s.

Remark 6.2. The function (41) is designed in such a way that it provides us with the possibility to capture two dissimilar experimentally observed scenarios, see Section 6.3.

6.1. Comparison of models

Let us start with the identification of parameters for the three models proposed in Table 1 using the experimental data from Section 4 and following the optimisation procedure suggested in Section 5.

We take the average of the four measurements as the base for finding the initial guess of parameters $m^{(0)}$ for each of the models. In particular, we fit the mean deflection angle by (42) to get the angular

---

[8] We optimise the parameters by solving the nonlinear least square problem with the constraint $b > 0$, again by routines implemented in SciPy.

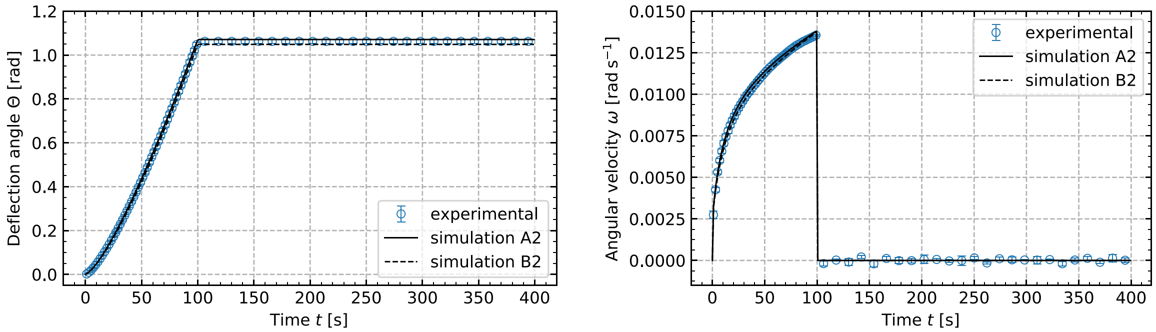

Fig. 6. Simulation inputs for the optimisation of model parameters. The measured deflection angle is fitted by the formula (42) which yields the angular velocity (43). Reported height of the samples: $H_{\mathrm{A2}} = 4.798\ \mathrm{mm}$, $H_{\mathrm{B2}} = 4.830\ \mathrm{mm}$.

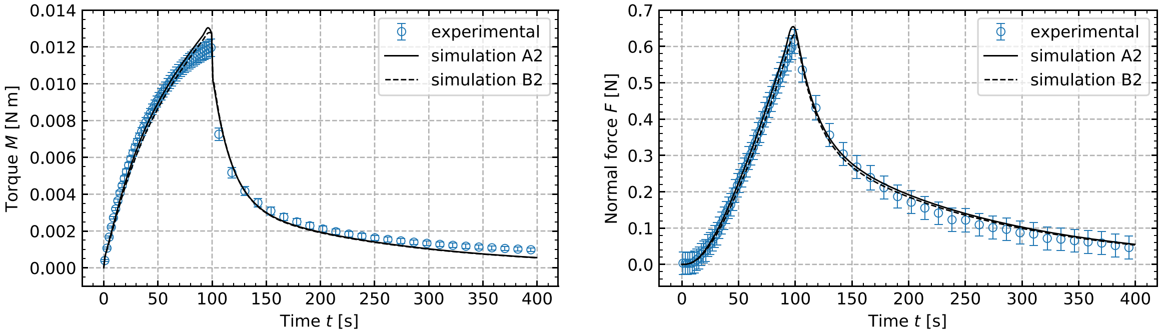

Fig. 7. Simulated torque $M(t; \mathcal{M}_{\mathrm{LL}}, m^*_{\mathrm{LL}})$ and normal force $F(t; \mathcal{M}_{\mathrm{LL}}, m^*_{\mathrm{LL}})$, computed for the inputs from Fig. 6 using the parameter values from Table 3.

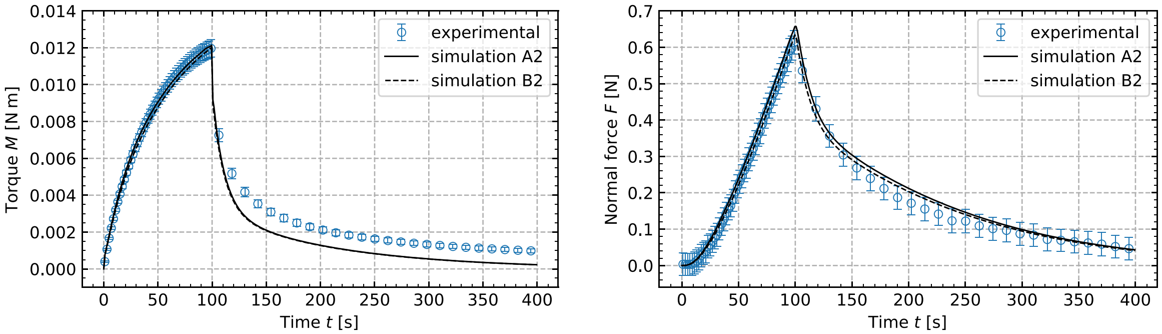

Fig. 8. Simulated torque $M(t; \mathcal{M}_{\mathrm{NN}}, m^*_{\mathrm{NN}})$ and normal force $F(t; \mathcal{M}_{\mathrm{NN}}, m^*_{\mathrm{NN}})$, computed for the inputs from Fig. 6 using the parameter values from Table 3.

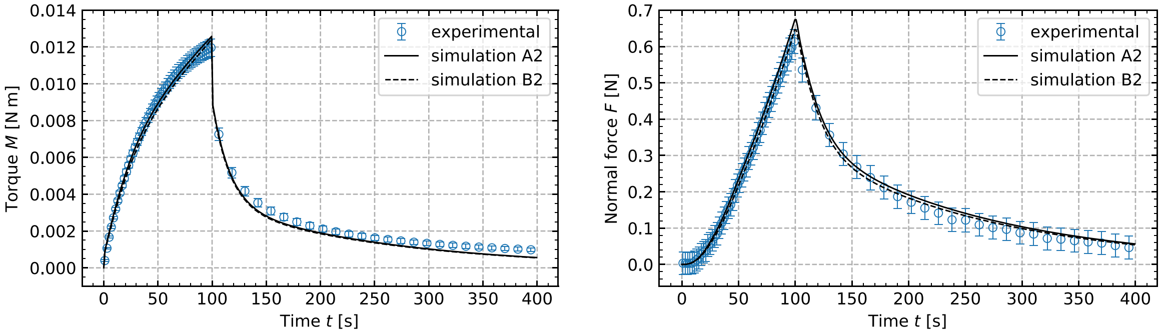

Fig. 9. Simulated torque $M(t; \mathcal{M}_{\mathrm{LN}}, m^*_{\mathrm{LN}})$ and normal force $F(t; \mathcal{M}_{\mathrm{LN}}, m^*_{\mathrm{LN}})$, computed for the inputs from Fig. 6 using the parameter values from Table 3.

velocity in the form (43). With this in hand, we run the TPE algorithm limited to 2 000 steps with the aim to minimise the cost functional (36) using a single set of data ($N = 1$) that consists of the mean torque and the mean normal force. All plots in Figs. 6–9 show the mean experimental data equipped by the standard deviation error bars which are supplemented by the estimated instrumental errors in case of the torque and normal force data (see Section 4.3).

With the initial guess obtained by fitting the mean data, we run the "restarted" Nelder–Mead algorithm with the aim to simultaneously

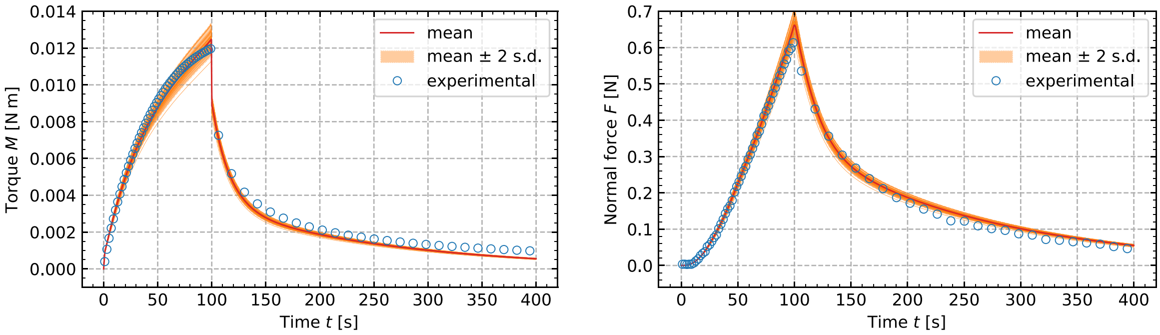

Fig. 10. Monte-Carlo simulation result showing the variance of the output with respect to changing radius of the sample ($R = 10 \pm 0.1$ mm, normal distribution). The simulation was carried out using the model $\mathcal{M}_{\mathrm{LN}}$ with optimised parameter values m^*_{LN} from Table 3.

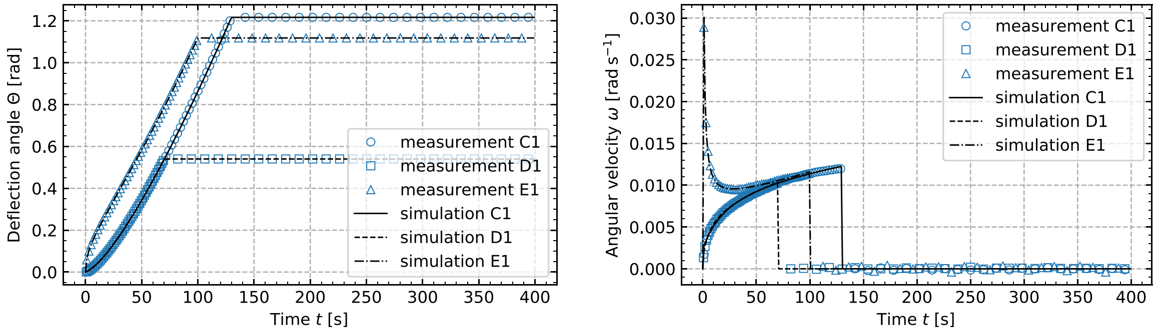

Fig. 11. Testing configurations, cf. Fig. 6. Reported height of the samples: $H_{\mathrm{C1}} = 4.169$ mm, $H_{\mathrm{D1}} = 4.168$ mm, $H_{\mathrm{E1}} = 4.302$ mm.

fit the data coming from two different measurements,[9] namely {A2, B2}. Our main objective remains the same: to minimise the cost functional (36), but this time using the two sets of observed data ($N = 2$). We fit the deflection angle data by (42), for each measurement separately, to get a couple of angular velocities in the form (43), see Fig. 6. These functions are subsequently considered as inputs for the numerical computation of $M(t; \mathcal{M}, m)$ and $F(t; \mathcal{M}, m)$ corresponding to the individual measurements, see (31) and (33).

Table 3 lists the optimised parameter values together with their initial guess found by the TPE algorithm. The corresponding values of the cost functional (36) are contained in the rightmost column. Based on these values, we are tempted to choose the optimal model $\mathcal{M}^* = \mathcal{M}_{\mathrm{LN}}$ in accordance with (39). Before doing so, let us explore the functions $M(t; \mathcal{M}_{\mathrm{label}}, m^*_{\mathrm{label}})$ and $F(t; \mathcal{M}_{\mathrm{label}}, m^*_{\mathrm{label}})$ for $\mathrm{label} \in \{\mathrm{LL}, \mathrm{NN}, \mathrm{LN}\}$ which are shown in Figs. 7–9.

First and foremost, all three models capture the jump response in the torque that is experimentally observed at the critical time t_0 as a consequence of the step change of the angular velocity. The model $\mathcal{M}_{\mathrm{LL}}$ fits the experimental data almost perfectly with only a slight overshoot of the torque data in the vicinity of the critical time t_0. There is no such overshoot in case of the model $\mathcal{M}_{\mathrm{NN}}$ which has the shear thinning property in contrast to $\mathcal{M}_{\mathrm{LL}}$, see Table 2. On the other hand, we clearly see that the model $\mathcal{M}_{\mathrm{NN}}$ undershoots the torque data in the second time segment during the relaxation stage. Finally, the model $\mathcal{M}_{\mathrm{LN}}$ combines the properties of both previous models and fits the experimental data the best.

Remark 6.3. Using the alternative cost functional introduced in Remark 5.1, we end up with qualitatively identical results.

6.2. Sensitivity analysis

In this section, we study the influence of the radius of the sample on the expected output using the Monte-Carlo approach, see e.g. Caflisch [35]. The experimental data shown in Fig. 10 represent the average data from Fig. 5. The mean value of the recorded deflection angle from Fig. 4 was used to get the input for the simulation. The results support our previous statement regarding the observed inconsistency in the measured torque, see Fig. 5 and the discussion at the end of Section 4.3. Indeed, we see that a relatively small change of the radius of the sample, which is still assumed to coincide with the radius of the plates, leads to a variance in the simulated torque that is both qualitatively and quantitatively comparable with the variance in the experimental data.

6.3. Tests with modified configurations

The aim of this section is to illustrate the capability of the models to make predictions in configurations other than the one used for the parameter fitting, see Fig. 6. These so-called *testing configurations* are captured in Fig. 11.

The testing scheme is the same as in the previous case, but different times for the ramping of the deflection angle were used in case of measurements C1 and D1. On the other hand, in the remaining case we used exactly the same setting as in the fitting configuration. However, the ramping was done in a completely different – but also repeatable – path in this particular case. Indeed, looking at Fig. 11, we see that the upper plate rotated fast at the beginning of the measurement E1 (for $t \ll t_0$) and slowed down as the time increased. This is in contrast with all other cases, where the rotation was gradually accelerated.

Remark 6.4. The testing configurations are in the same rotational rheometer geometry as the one used in the parameter fitting. To test the full predictive power of the model it would be prudent for future work to test in a different geometry, e.g. capillary rheometer.

---

[9] We intentionally choose measurements characterising the variance in the data, in order to mitigate the risk of fitting data with higher experimental error.

Table 3
Output of TPE algorithm subsequently used as the initial guess in the restarted Nelder–Mead algorithm, and the final optimised parameter values for models listed in Table 1.

	μ_0 [Pa s]	μ_1 [Pa s]	μ_2 [Pa s]	G_1 [Pa]	G_2 [Pa]	λ_1 [s]	λ_2 [s]	$J(\mathcal{M}, m^*)$
$m^{(0)}_{\mathrm{LL}}$	4.70E+04	1.95E+05	1.61E+05	1.66E+03	9.34E+03	1.18E+02	1.72E+01	4.57E−01
m^{*}_{LL}	4.95E+04	2.15E+05	1.74E+05	1.33E+03	1.01E+04	1.61E+02	1.73E+01	3.88E−01
$m^{(0)}_{\mathrm{NN}}$	8.12E+04	9.09E+04	2.22E+05	8.86E+03	2.60E+03	1.03E+01	8.53E+01	5.16E−01
m^{*}_{NN}	6.17E+04	1.35E+05	2.16E+05	1.30E+04	1.94E+03	1.04E+01	1.11E+02	4.43E−01
$m^{(0)}_{\mathrm{LN}}$	9.70E+04	2.35E+05	1.01E+05	1.80E+03	5.83E+03	1.31E+02	1.73E+01	4.34E−01
m^{*}_{LN}	7.98E+04	2.08E+05	1.43E+05	1.27E+03	8.77E+03	1.64E+02	1.63E+01	3.44E−01

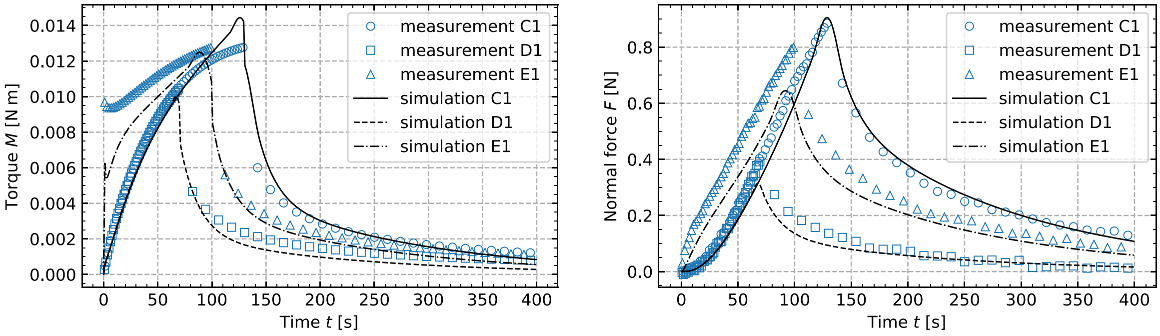

Fig. 12. Simulated torque $M(t; \mathcal{M}_{\mathrm{LL}}, m^*_{\mathrm{LL}})$ and normal force $F(t; \mathcal{M}_{\mathrm{LL}}, m^*_{\mathrm{LL}})$, computed for the inputs from Fig. 11 using the parameter values from Table 3.

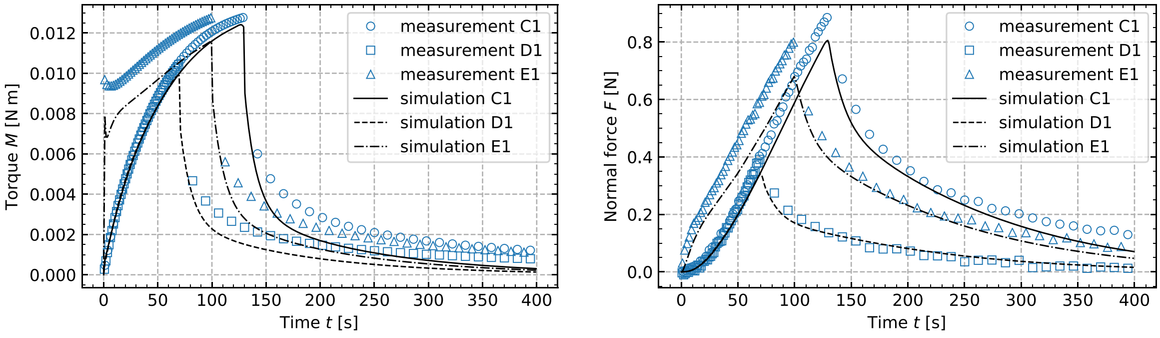

Fig. 13. Simulated torque $M(t; \mathcal{M}_{\mathrm{NN}}, m^*_{\mathrm{NN}})$ and normal force $F(t; \mathcal{M}_{\mathrm{NN}}, m^*_{\mathrm{NN}})$, computed for the inputs from Fig. 11 using the parameter values from Table 3.

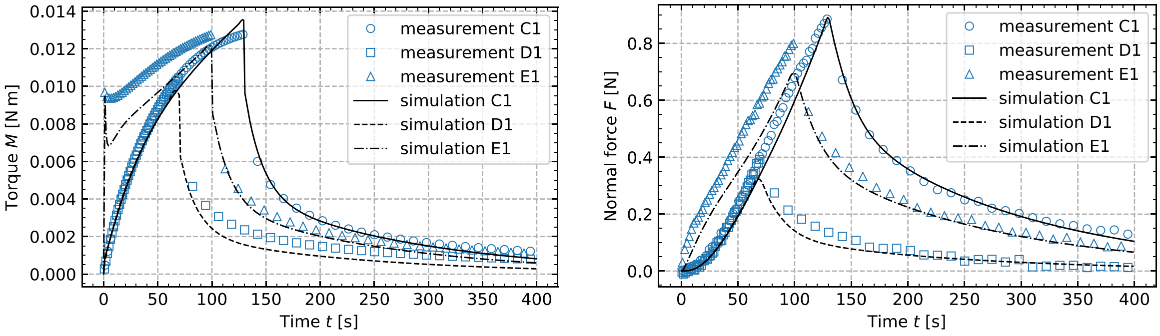

Fig. 14. Simulated torque $M(t; \mathcal{M}_{\mathrm{LN}}, m^*_{\mathrm{LN}})$ and normal force $F(t; \mathcal{M}_{\mathrm{LN}}, m^*_{\mathrm{LN}})$, computed for the inputs from Fig. 11 using the parameter values from Table 3.

Comparison of the simulation results with the experimental data for individual models is shown in Figs. 12–14. Recall that the computation of $M(t; \mathcal{M}, m)$ and $F(t; \mathcal{M}, m)$ is based on the numerical solution of the system of ODEs (28) that was derived under certain simplifying assumptions. The acceleration observed at the start-up of measurement E1 makes some of these assumptions irrelevant. Moreover, the choice of the initial conditions (29) is not suitable in this specific case. In order to make them acceptable, we allow a fast ramping of the angular velocity to a specified value within the first few time steps. Due to these inaccuracies one cannot expect an ideal fit of the experimental data for this particular measurement in the time segment $(0, t_0]$. Let us conclude with the observation that the model $\mathcal{M}_{\mathrm{LN}}$ provides us with a satisfactory prediction of the response of the SBR in different torsional flow configurations.

7. Conclusions

By performing the experiment described in Section 4, we have observed that the response of the uncured SBR is qualitatively comparable with the response of asphalt binders, especially in the context of the work by Narayan et al. [30]. Such an observation led us to the idea to describe the complicated nonlinear viscoelastic response of SBR by one of the models recently discussed by Málek et al. [11,12]. We compared two existing models, here denoted by $\mathcal{M}_{\mathrm{LL}}$ and $\mathcal{M}_{\mathrm{NN}}$, with the newly proposed variant $\mathcal{M}_{\mathrm{LN}}$ (the derivation is sketched in Section 2.3), see Table 1.

The first two models showed a relatively good match between the simulated data and the experimental data, with only a few imperfections especially in the torque data. Possible reasons which make the two models imperfect in the given configuration may be related to the following facts. First, $\mathcal{M}_{\mathrm{LL}}$ cannot describe shear thinning behaviour which was experimentally proven for SBR, see e.g. Mourniac et al. [36]. Second, $\mathcal{M}_{\mathrm{NN}}$ describes the material as being "fully incompressible" which may be inappropriate in case of SBR. On the other hand, $\mathcal{M}_{\mathrm{NN}}$ captures shear thinning and the derivation of $\mathcal{M}_{\mathrm{LL}}$ is based on the assumption that the material stores the elastic energy as a compressible neo-Hookean solid. The new model combines physical properties of both in an appropriate way. In particular, it can describe shear thinning behaviour and a part of the elastic energy is stored as in the case of a compressible neo-Hookean solid, see (15). Probably this makes $\mathcal{M}_{\mathrm{LN}}$ superior to the other two models in predicting the behaviour of SBR in the chosen fitting and testing configurations.

For models investigated in this work, we have observed that step changes (discontinuous jumps) in the input angular velocity lead to the corresponding step changes in the simulated torque, see Figs. 6–9 and 11–14. It seems to plausibly reflect the experimentally observed behaviour. Rigorous analysis of the response of nonlinear materials to step inputs is feasible within the framework of Colombeau algebra, see Řehoř et al. [37] and Průša et al. [38].

Another line for future investigation would be to investigate the validity of the new model and the fitted parameters in a completely different geometrical configuration, e.g. a capillary rheometer. Furthermore, only unfilled SBR at a fixed temperature was studied in this paper. The influence of different fillers in SBR compounds as well as the influence of the temperature on model parameters should be subject to further intensive research.

Supplementary materials

The full code and data to produce all of the figures in this paper is available at [39] (https://doi.org/10.6084/m9.figshare.7993205.v2), along with a Docker image (see [40] for details) to execute it in.

Declaration of competing interest

The authors declare that they have no known competing financial interests or personal relationships that could have appeared to influence the work reported in this paper.

Acknowledgements

This work was funded by the Luxembourg National Research Fund with grant C-PPP17/MS/11617214/SLIPEX in the CORE-PPP programme.

References

[1] C. Rauwendaal, Polymer Extrusion, Carl Hanser Verlag GmbH Co KG, 2014, http://dx.doi.org/10.3139/9781569905395.

[2] Y. Nakajima, Advanced Tire Mechanics, Springer, 2019, http://dx.doi.org/10.1007/978-981-13-5799-2.

[3] F. Carleo, E. Barbieri, R. Whear, J.J.C. Busfield, Limitations of viscoelastic constitutive models for carbon-black reinforced rubber in medium dynamic strains and medium strain rates, 10 (9) (2018) 988, http://dx.doi.org/10.3390/polym10090988.

[4] S. Montes, J.L. White, N. Nakajima, Rheological behavior of rubber carbon black compounds in various shear flow histories, 28 (2) (1988) 183–212, http://dx.doi.org/10.1016/0377-0257(88)85039-0.

[5] C. Ovalle Rodas, F. Zaïri, M. Naït-Abdelaziz, P. Charrier, Temperature and filler effects on the relaxed response of filled rubbers: Experimental observations on a carbon-filled SBR and constitutive modeling, 58 (2015) 309–321, http://dx.doi.org/10.1016/j.ijsolstr.2014.11.001.

[6] M. Jugo Viloria, M. Valtier, B. Vergnes, Volume instabilities in capillary flow of pure SBR and SBR compounds, J. Rheol. 61 (5) (2017) 1085–1097, http://dx.doi.org/10.1122/1.4999061.

[7] S.H. Choi, M.-Y. Lyu, Application of the PTT model for capillary extrusion of rubber compounds, Int. Polym. Process. 24 (4) (2009) 326–333, http://dx.doi.org/10.3139/217.2172.

[8] N.A. Talib, Ö. Ertunç, Application of Giesekus Model for capillary extrusion of rubber compound, 52 (2) 185–193, http://dx.doi.org/10.1252/jcej.18we070.

[9] M. Shabani, K. Jahani, M. Di Paola, M.H. Sadeghi, Frequency domain identification of the fractional Kelvin-Voigt's parameters for viscoelastic materials, 137 (2019) 103099, http://dx.doi.org/10.1016/j.mechmat.2019.103099.

[10] G. Alotta, O. Barrera, A. Cocks, M. Di Paola, The finite element implementation of 3D fractional viscoelastic constitutive models, 146 (2018) 28–41, http://dx.doi.org/10.1016/j.finel.2018.04.003.

[11] J. Málek, K.R. Rajagopal, K. Tůma, A thermodynamically compatible model for describing the response of asphalt binders, Int. J. Pavement Eng. 16 (4) (2015) 297–314, http://dx.doi.org/10.1080/10298436.2014.942860.

[12] J. Málek, K.R. Rajagopal, K. Tůma, Derivation of the variants of the Burgers model using a thermodynamic approach and appealing to the concept of evolving natural configurations, Fluids 3 (4) (2018) 69, http://dx.doi.org/10.3390/fluids3040069.

[13] K.R. Rajagopal, A.R. Srinivasa, A thermodynamic frame work for rate type fluid models, J. Non-Newton. Fluid Mech. 88 (3) (2000) 207–227, http://dx.doi.org/10.1016/S0377-0257(99)00023-3.

[14] M. Freund, H. Lorenz, D. Juhre, J. Ihlemann, M. Klüppel, Finite element implementation of a microstructure-based model for filled elastomers, 27 (6) (2011) 902–919, http://dx.doi.org/10.1016/j.ijplas.2010.10.003.

[15] J.M. Burgers, Mechanical considerations—Model systems—Phenomenological theories of relaxation and viscosity, in: First Report on Viscosity and Plasticity, Nordemann Publishing, New York, NY, USA, 1939, pp. 5–67, Chapter 1.

[16] J. Bergstra, D. Yamins, D.D. Cox, Making a science of model search: Hyperparameter optimization in hundreds of dimensions for vision architectures, in: JMLR Workshop and Conference Proceedings, Atlanta, Gerorgia, 2013, pp. 115–123, URL: https://dash.harvard.edu/handle/1/12561000.

[17] J.A. Nelder, R. Mead, A simplex method for function minimization, Comput. J. 7 (4) (1965) 308–313, http://dx.doi.org/10.1093/comjnl/7.4.308.

[18] L.H.O. Hellström, M.A. Samaha, K.M. Wang, A.J. Smits, M. Hultmark, Errors in parallel-plate and cone-plate rheometer measurements due to sample underfill, Meas. Sci. Technol. 26 (1) (2014) 015301, http://dx.doi.org/10.1088/0957-0233/26/1/015301.

[19] K.R. Rajagopal, Remarks on the notion of "pressure", Int. J. Non-Linear Mech. 71 (2015) 165–172, http://dx.doi.org/10.1016/j.ijnonlinmec.2014.11.031.

[20] J.M. Krishnan, K.R. Rajagopal, Review of the uses and modeling of bitumen from ancient to modern times, Appl. Mech. Rev. 56 (2) (2003) 149–214, http://dx.doi.org/10.1115/1.1529658.

[21] S.P.A. Narayan, D.N. Little, K.R. Rajagopal, Nonlinear viscoelastic model for describing the response of asphalt binders within the context of a Gibbs-Potential–based thermodynamic framework, J. Eng. Mech. 141 (2) (2015) 04014116, http://dx.doi.org/10.1061/(ASCE)EM.1943-7889.0000682.

[22] S.P.A. Narayan, D.N. Little, K.R. Rajagopal, Modelling the nonlinear viscoelastic response of asphalt binders, Int. J. Pavement Eng. 17 (2) (2016) 123–132, http://dx.doi.org/10.1080/10298436.2014.925621.

[23] J. Málek, K.R. Rajagopal, K. Tůma, A thermodynamically compatible model for describing asphalt binders: solutions of problems, Int. J. Pavement Eng. 17 (6) (2016) 550–564, http://dx.doi.org/10.1080/10298436.2015.1007575.

[24] J.G. Oldroyd, On the formulation of rheological equations of state, Proc. R. Soc. Lond. Ser A. Math. Phys. Sci. 200 (1063) (1950) 523–541, http://dx.doi.org/10.1098/rspa.1950.0035.

[25] A.I. Leonov, Nonequilibrium thermodynamics and rheology of viscoelastic polymer media, Rheol. Acta 15 (2) (1976) 85–98, http://dx.doi.org/10.1007/BF01517499.

[26] A.N. Beris, B.J. Edwards, Thermodynamics of Flowing Systems: with Internal Microstructure, Oxford University Press, 1994.

[27] J. Málek, V. Průša, Derivation of equations for continuum mechanics and thermodynamics of fluids, in: Y. Giga, A. Novotný (Eds.), Handbook of Mathematical Analysis in Mechanics of Viscous Fluids, Springer, Cham, 2016, pp. 1–70, http://dx.doi.org/10.1007/978-3-319-10151-4_1-1.

[28] E. Jones, T. Oliphant, P. Peterson, et al., SciPy: Open source scientific tools for Python, 2001, URL: http://www.scipy.org/. [Online; accessed 28/08/2019].

[29] A. Gansen, M. Řehoř, C. Sill, P. Polińska, S. Westermann, J. Dheur, J.S. Hale, J. Baller, Investigation of the Sharkskin melt instability using optical Fourier analysis, J. Appl. Polym. Sci. 137 (24) (2020) 48806, http://dx.doi.org/10.1002/app.48806.

[30] S.P.A. Narayan, J.M. Krishnan, A.P. Deshpande, K.R. Rajagopal, Nonlinear viscoelastic response of asphalt binders: An experimental study of the relaxation of torque and normal force in torsion, Mech. Res. Commun. 43 (2012) 66–74, http://dx.doi.org/10.1016/j.mechrescom.2012.02.012.

[31] D. Colton, H.W. Engl, A.K. Louis, J. McLaughlin, W. Rundell, Surveys on Solution Methods for Inverse Problems, Springer Science & Business Media, 2012, http://dx.doi.org/10.1007/978-3-7091-6296-5.

[32] A. Gelman, J.B. Carlin, H.S. Stern, D.B. Dunson, A. Vehtari, D.B. Rubin, J.B. Carlin, H.S. Stern, D.B. Dunson, A. Vehtari, D.B. Rubin, Bayesian Data Analysis, Chapman and Hall/CRC, 2013, http://dx.doi.org/10.1201/b16018.

[33] A.M. Stuart, Inverse problems: A Bayesian perspective, 19 (2010) 451–559, http://dx.doi.org/10.1017/S0962492910000061.

[34] J.C. Lagarias, J.A. Reeds, M.H. Wright, P.E. Wright, Convergence properties of the Nelder–Mead simplex method in low dimensions, 2006, http://dx.doi.org/10.1137/S1052623496303470.

[35] R.E. Caflisch, Monte Carlo and Quasi-Monte Carlo methods, Acta Numer. 7 (-1) (1998) 1–49, http://dx.doi.org/10.1017/S0962492900002804.

[36] P. Mourniac, J.F. Agassant, B. Vergnes, Determination of the wall slip velocity in the flow of a SBR compound, Rheol. Acta 31 (6) (1992) 565–574, http://dx.doi.org/10.1007/BF00367011.

[37] M. Řehoř, V. Průša, K. Tůma, On the response of nonlinear viscoelastic materials in creep and stress relaxation experiments in the lubricated squeeze flow setting, Phys. Fluids 28 (10) (2016) 103102, http://dx.doi.org/10.1063/1.4964662.

[38] V. Průša, M. Řehoř, K. Tůma, Colombeau algebra as a mathematical tool for investigating step load and step deformation of systems of nonlinear springs and dashpots, Z. Angew. Math. Phys. 68 (1) (2017) 24, http://dx.doi.org/10.1007/s00033-017-0768-x.

[39] M. Řehoř, A. Gansen, J.S. Hale, A comparison of constitutive models for describing the flow of uncured styrene-butadiene rubber - Supplementary material, 2020, http://dx.doi.org/10.6084/m9.figshare.7993205.v2.

[40] J.S. Hale, L. Li, C.N. Richardson, G.N. Wells, Containers for portable, productive, and performant scientific computing, 19 (6) (2017) 40–50, http://dx.doi.org/10.1109/MCSE.2017.2421459.